Results in Optics 13 (2023) 100524

Contents lists available at ScienceDirect

Results in Optics

journal homepage: www.elsevier.com/locate/rio

Designing a sky-scanning Fabry–Perot interferometer system with a large size integrating sphere

Prasanna Mahavarkar [a,*], S. Sriram [b], Bhagyashree Joshi [c], Amirul Hasan [b], Remya B.S. [b], Sarvesh Chandra [a]

[a] Indian Institute of Geomagnetism, Plot No. 5, Sector 18, New Panvel, Navi Mumbai 410 218, India
[b] Indian Institute of Astrophysics, II Block, Koramangala, Bengaluru, 560 034, India
[c] Savitribai Phule Pune University, Ganeshkhind Road, Pune 411 007, India

ARTICLE INFO

Keywords:
Integrating sphere
CCD
Optical simulation

ABSTRACT

Integrating spheres can be manufactured at sizes ranging from 1 mm to 3 m in diameter. It has been agreed widely by manufacturers that fitting a large-sized integrating sphere as per the customer requirement is a complex process. Thus, these spheres due to its large beam divergence from the exit port, have never been deployed for the calibration of aeronomy applications. In this article a optical system is described to integrate a large-sized integrating sphere with the Fabry–Perot etalon and thus devise a set-up to generate the concentric ring pattern and record it on the detector. The experimental set-up was verified by optical simulation using ZEMAX (OpticStudio) so as to validate the system's performance in the laboratory. The important parameter finesse is calculated and its accuracy is found to be 80%.

1. Introduction

An integrating sphere (IS) is an optical component that is a hollow spherical cavity with its interior walls coated with a diffuse white reflective coating. Thus, it acts like a diffuser, preserving power but neglecting spatial information. Light entering the sphere undergoes multiple scattering reflections, so that rays that are incident on any point on the inner surface are equally distributed, minimizing the effects of the original direction of the rays. These spheres are available with a wide range of specifications and can be configured with a number of applications (https://www.laserfocusworld.com/test-measurement/test-measurement/article/16567486/product-focus-integrating-spheres-how-to-select-an-integrating-sphere-for-your-application) such as spectroscopy (Hanssen and Snail, 2002), reflectance measurements (Lindseth et al., 1999), measurement of emission from light sources (Hodgkinson et al., 2009), calibration of air-glow instruments (Shiokawa et al., 2012; yuki Yamamoto et al., 2002; Wang et al., 2020; Gelderman et al., 1995; Anderson et al.), measuring the optical properties of tissues (Pickering et al., 1993), and etc.

The small-sized spheres are less expensive, necessarily have smaller utility ports and very high throughput. The throughput may be so high, depending on the light source, that neutral density filters or fibre optic cables are required to prevent detector saturation. The port fraction of these spheres is also high. Consequently, the measurement data generated from a small-sized integrating sphere will be less accurate than the same application using a large-sized integrating sphere. On the other hand, the large-sized integrating sphere exhibits less throughput than the smaller one and larger optical attenuation, thereby introducing a higher signal-to-noise ratio. These spheres are more expensive to manufacture and the beam divergence from the exit port is large and thus have never been deployed for calibration of aeronomy instruments. This article discusses a method to generate a uniform source beam from a largely diverging beam delivered by a large-sized integrating sphere as a source and capture the resulting interference fringes generated from the Fabry–Perot etalon on the detector.

The optical modelling for such an system has been done with ZEMAX (OpticStudio) and, accordingly, the specifications and working distances have been incorporated into the system.

2. Experimental setup

Figure (Fig. 1) shows the optical arrangement in the laboratory and Fig. 2 shows the schematic of the set-up. An integrating sphere collects a beam from a source located external to the input port of the sphere and outputs a nearly diverging beam from the exit port. Thus, it is configured to be used as a light source. The beam exiting the sphere is first collected by a sky-scanning mirror making an angle of 45° to the incident light. This light then passes through the first achromat L_1 and is

* Corresponding author.
E-mail address: mahavarkarprasanna@gmail.com (P. Mahavarkar).

https://doi.org/10.1016/j.rio.2023.100524
Received 13 December 2022; Received in revised form 18 August 2023; Accepted 1 September 2023
Available online 6 September 2023
2666-9501/

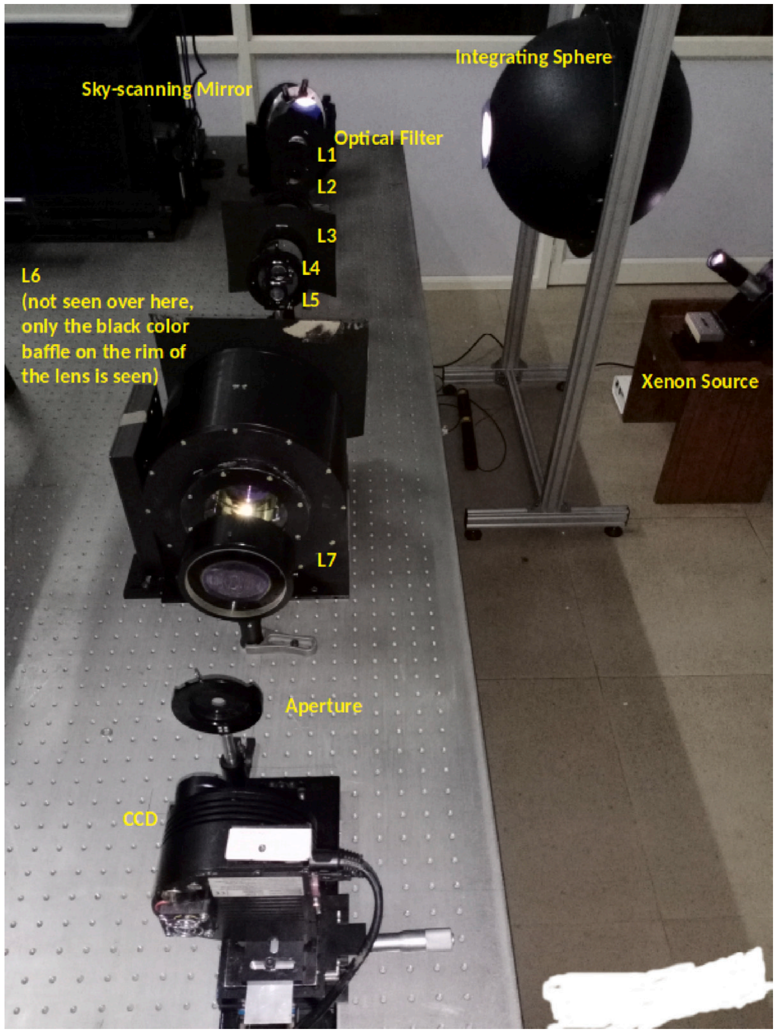

Fig. 1. Optical set-up at the Photonics Laboratory of the Indian Institute of Astrophysics, Bengaluru India. The integrating sphere was fed by a HeNe laser (632.8 nm) and a Xenon source respectively.

collected by an achromat L_3 introducing the angular magnification for collecting light from the far placed exit port of the integrating sphere according to the ratio of focal lengths of L_1 and L_3. This arrangement is similar to the telescope. The field lens L_2 in the intermediate image plane avoids vignetting, as even the light rays at moderate angles those of these cannot enter L_3 to reach the successive optics (https://www.rp-photonics.com/field_lenses.html, http://www.sk-advanced.com/category/chapter-5-feild-lenses). The light from L_3 is collected by the achromat L_4 which now forms the objective achromat L_4. The dimensions of this achromat is so chosen that it approximately matches the diameter of L_3 and the focal length brings in an angular field of view (AFOV) 5° (= $\tan^{-1}$ (13.312/150.00)) necessary for traditional type of scanning interferometers that use mirrors to observe a specific area in the sky. The light is then focused on the second focal point formed by the achromat L_4. A thin plate with a circular hole and another field lens (achromat) L_5 is located on this focal plane. The light then expands towards the achromat L_6. The field lens, L_5 is inserted to avoid vignetting due to expansion of the light towards L_6. Also, L_5 is set just below the focal point C to avoid imaging any dust or scratches on the L_5 achromat on the final CCD plane. The large diameter achromat L_6 (ϕ = 110 mm) with the focal length, f = 300 mm, makes the wavefront of the light towards the sealed etalon become nearly parallel with a maximum incident angle of 1.3° (= $\tan^{-1}$ (13.312/300.0)/2). The transmitted light then passes through the etalon and is focused onto the CCD plane by the achromat L_7. The CCD size is 10 mm × 10 mm with 500 × 500 pixels, and a pixel dimension of 10 μm. The optics from the focal plane of L_5 to the plane of the detector forms a symmetric system centred on the etalon. The optical arrangement from the achromat L_4 to the CCD plane is referred to as the telecentric architecture of the Fabry–Perot interferometer.

3. The optical and opto-mechanical components

The optical arrangement comprises the integrating sphere fed by a laser source, sky-scanning mirror, plano-convex lens, achromatic lens, a thin plate with an aperture, Fabry–Perot etalon and a Charge-coupled device (CCD). The integrating sphere is fed by a 632.8 nm laser source (Figs. 3 and 5) procured from Edmund optics (https://www.edmundoptics.in/p/model-1125-5mw-random-polarization-lumentum-hene-laser/17370/) and manufactured by Lumentum. The beam diameter is 0.81 mm and it delivers an output power of 5 mW. For feeding the beam into the integrating sphere, the laser is just placed close to one of the input ports of the sphere.

The integrating sphere is a custom-made component of the diameter of 500 mm. It has 2 input ports each of diameter 50 mm with a baffle and one output port of diameter 120 mm. The internal surface is coated with a special water based Barium Sulphate ($BaSO_4$) (R98) white reflective paint particularly suitable for internal coating of integrating spheres and black enamel paint outside (textured finish). The sphere was the first to be simulated in ZEMAX (OpticStudio) to confirm

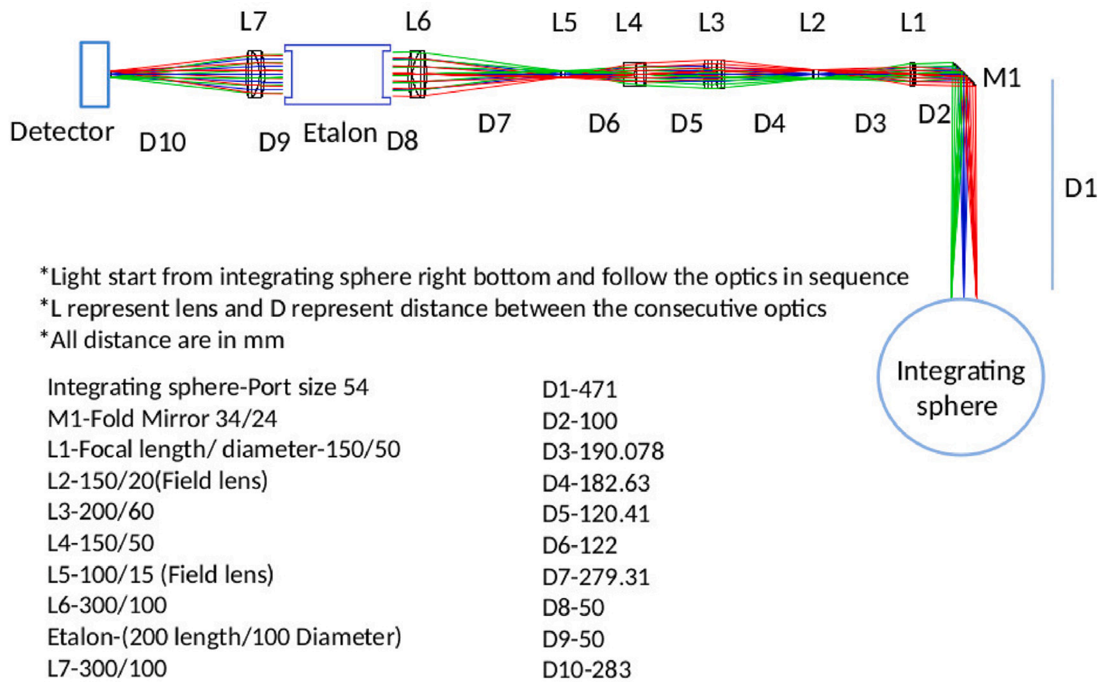

Fig. 2. The schematic of the optical set-up with the dimensions of every component utilized in the design.

Fig. 3. Laser source.

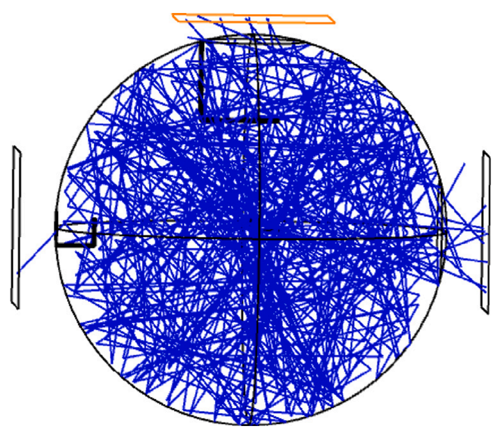

Fig. 4. Optical simulation of the integrating sphere in ZEMAX (OpticStudio).

its behaviour in the optical system (Fig. 4). Next, a white piece of paper was placed close to the sphere's exit port and then moved away from the port as part of a manual (basic) test to determine the beam collimation. Visual observation revealed that as the paper moved away from the port, the beam intensity rapidly decreased and the diameter of the spot increased, indicating the beam's diverging nature from the sphere's exit port.

An aluminium support to the sphere is provided to elevate it to the level of the optical table for testing. The structure is held with fixtures of stainless steel bolts (M5) and corrosion protective coatings (https://www.jamesglen.com.au/finishes-and-coatings/) T channel nuts. Non-skid, cushioned heavy duty rubber leg tips are fitted into the legs of the mount (https://www.accurate-prod.com/standard-products/leg-tips/) (https://www.grainger.com/category/furniture-hospitality-and-food-service/furniture/indoor-furnishings/furniture-tips-and-caps) to protect floor from wear and tear and make the structure moving easier.

The beam is admitted into the sphere through one of the input ports and the hot spot is formed on the baffle. The baffle prevents direct radiation from the hot spot from exiting the exit port of the sphere. Thus, the total exiting beam is independent of polarization or beam alignment and is nearly diverging in nature. This beam is then collected by the sky-scanning mirror and passed on to the first achromat L_1 from where the process of collimating the beam is initiated.

The sky-scanning mirror is a custom-made mirror manufactured by Arksa Research Labs Pvt. Ltd, Bengaluru India (https://sites.google.com/site/arksalabs/home). It is circular shape geometry (Fig. 6) with a diameter of 76 mm and thickness of 25 mm. The mirror has the most popular mirror coating on a plano substrate with a polished back side. The front surface is coated with protected silver coating that offers > 96% average reflectance from 450 nm to 20 μm and the back side is polished to a $\lambda/6$ flatness with a surface quality (scratch-dig) of 40–20.

The sky-scanning mirror is mounted on a custom-made gimbal mount suitable for holding a fixed size mirror of ϕ = 76 mm. This mount provides a 360° coarse positioning on two axes of the mirror surface adjustments in addition to some fine adjustment. It is the first component in the optical system to receive the light beam exiting the exit port of the integrating sphere to reflect it on the first lens L_1 and further to the system. On the field (at the observation site) the mirror will scan the horizon at an elevation of 40°–45° from the

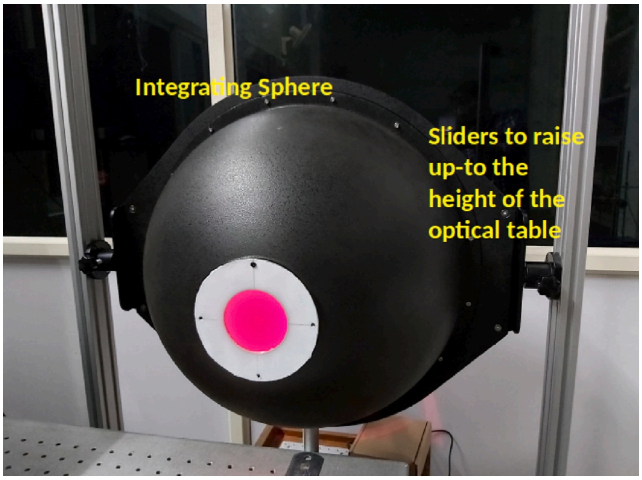

Fig. 5. The exit port of the integrating sphere is reduced from 120 mm to 76 mm to match the objective lens L_4 of the system that is responsible for creating the field-of-view (AFOV) 5° for the system.

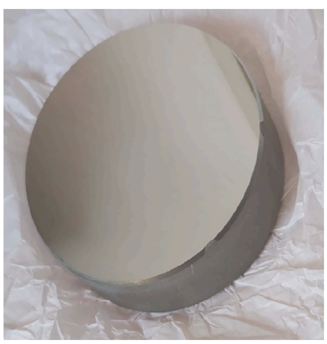

Fig. 6. Front coated mirror.

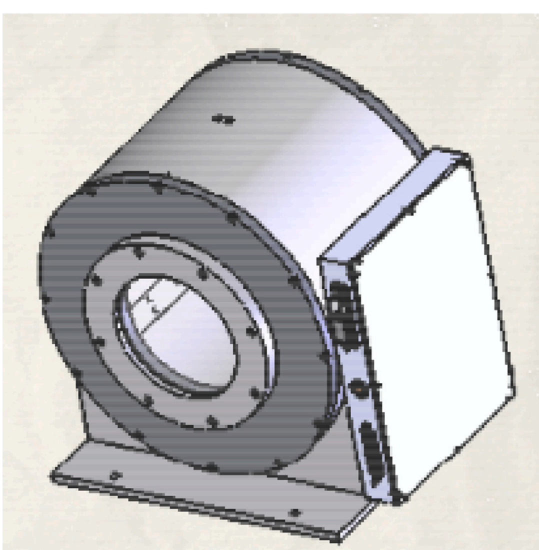

Fig. 7. Fabry–Perot etalon.

mounting base plate. The lens L_1 and the rest of the lenses in the system are plano-convex and achromatic lens that were procured from Edmund Optics (https://www.edmundoptics.com/) as per the required specifications except the collimating and the focusing lens, placed

Fig. 8. The CCD camera is fixed at the focal plane of the re-imaging lens L_7 to capture the image formed by the etalon.

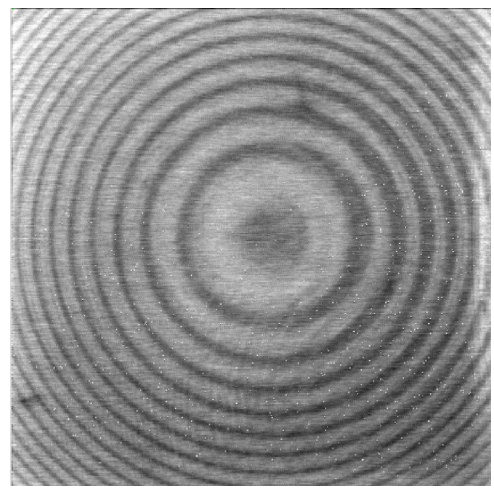

Fig. 9. Concentric ring pattern produced by Fabry–Perot etalon.

before and after the etalon, were custom made by Optica (https://www.opticsindia.com/) to match the usable area of the etalon. The respective part number with only the diameter and focal length is tabulated below (Table 1). The achromatic lenses were utilized in the design to reduce chromatic aberrations and improve the brightness and clarity of the image (https://www.opticsforhire.com/blog/achromatic-doublet-with-flint-crown-glass/). Also, unlike singlet lenses, the coaxial performance of achromatic lenses will not decrease as the aperture size increases, allowing to use the entire transparent aperture.

The optical configuration following the lens L_1 and the further components make the beam nearly collimated with a small incidence angle for the Fabry–Perot etalon to form the necessary interference pattern to be recorded on the detector. The tunable Fabry–Perot etalon with the controller unit was procured from Michigan Aerospace Corporation, USA (http://www.michiganaerospace.com/). Fig. 7 shows the CAD drawing of the Fabry–Perot etalon and Table 2 shows the specifications.

The detector CCD camera ST-9XEI (http://www.company7.com/library/sbig/sbwhtmls/stremoteup.htm) is a single sensor version with no internal guiding CCD. However, it does include the Remote Guiding Head Port for attachment of an optional external guiding head at any time. The imaging CCD (Fig. 8) is also Class 1 KAF-0261E with no column defects. It has been chosen as it has been a successful camera in its own right among those seeking a large field of view and high sensitivity at a relatively low cost. The camera uses a KAF-0261E CCD from Kodak with 512 × 512 pixels at 20 μm. KAF-0261E is a new high QE Class 1 imaging CCD with no column defects.

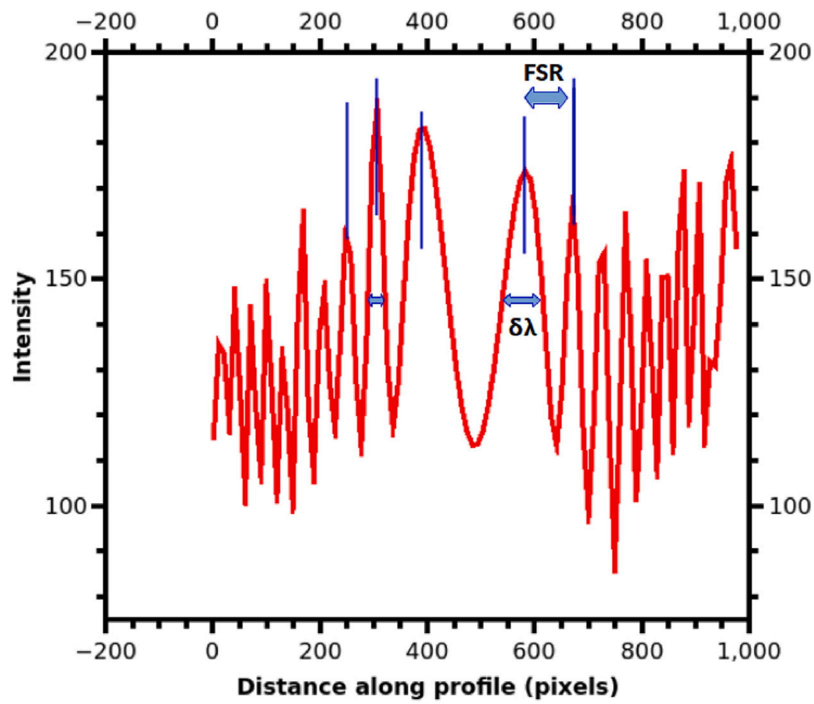

Fig. 10. Airy function for a given reflectance coefficient of the etalon. The intensity variation is in one of the best directions in the image.

Table 1
Specifications of the achromatic lens.

Make	Stock	Type	Diameter (mm)	Focal length (mm)	Coating
Edmund	49–391	Achromat	50	150	VIS-NIR
Edmund	47–386	Plano-Convex	20	150	VIS-NIR
Custom made	—	Achromat	60	200	VIS-NIR
Edmund	45–706	Plano-Convex	15	100	VIS-NIR
Optica	—	Achromat	100	300	VIS-NIR

Table 2
The etalon specifications.

Parameter	Specifications
Etalon Gap	1.5 cm
Etalon Clear Aperture	10.0 cm
Surface Quality	λ/200 @ 633 nm
Wavelength(s)	633 nm
Operating Temperature	10–50 °C

4. Results and discussion

For the incidence angle $\theta_i = 1.3°$ on the etalon and without varying any other parameter, maximum reflectivity can be obtained only at selected angles. Thus, when a conically diverging circular monocromatic beam illuminates a thin etalon, the projection of the transmitted radiation on a screen consists of well-defined concentric rings (Fig. 9). The width of the rings is defined by the finesse (F) of the etalon and the bandwidth of the incident radiation. The separation between adjacent rings is analogous to the free spectral range (*FSR*) (Laufer, 1996) and the performance of the etalon is characterized by these two parameters.

Fig. 9 shows about ten full fringes for a given reflectance value. The cross-section along the image gives the Airy function as shown in Fig. 10. The Fig. 11 is the better contrast image of the same Fig. 9 but with a slight tilt to the etalon. Such a tilt is necessary to compensate for the offset of plate parallelism within the etalon that may have occurred at the stage of manufacturing or incorrect mounting position over a period of time.

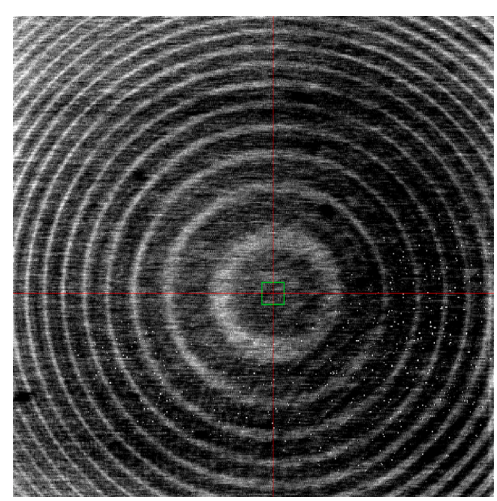

Fig. 11. The improvement in the image quality is achieved by providing a fine tilt to the etalon and blocking of the stray light leakage from the black curtains. This stray light is blocked by inserting black colour baffles on the rim of the lens used in the system.

The intensity distribution of the transmitted beam is given by Airy's formula (Jenkins and White 1937),

$$I = \frac{I_{max}}{1 + F sin^2(\delta/2)} \quad (1)$$

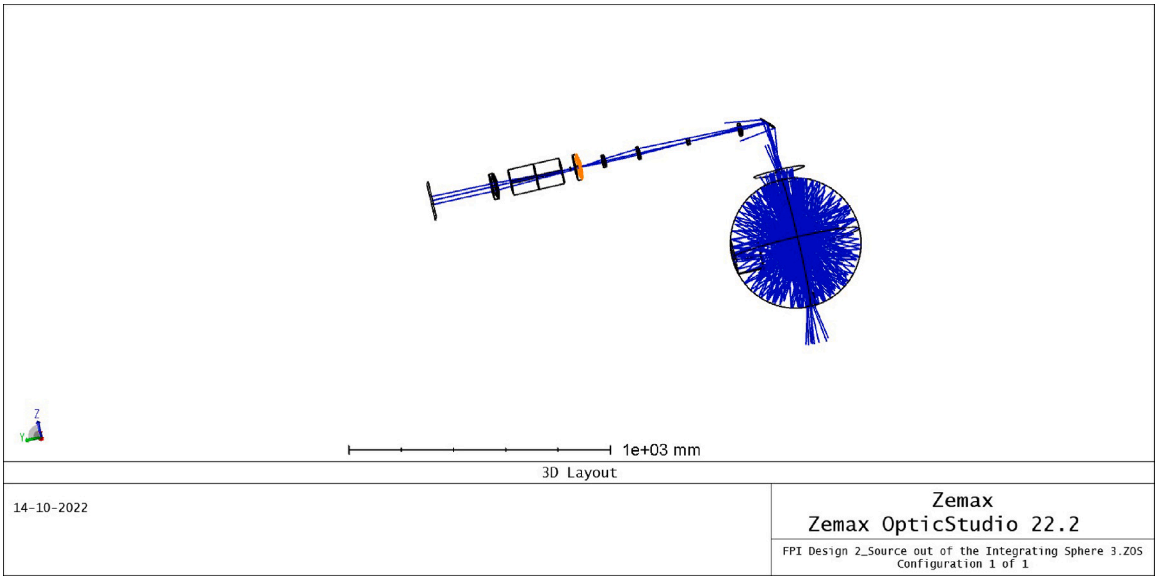

Fig. 12. The raytrace of the achromatic lens design shows the optical path starting from the integrating sphere to the detector. This system has 10 elements in 4 groups, with a focusing mechanism on the last lens before the sensor.

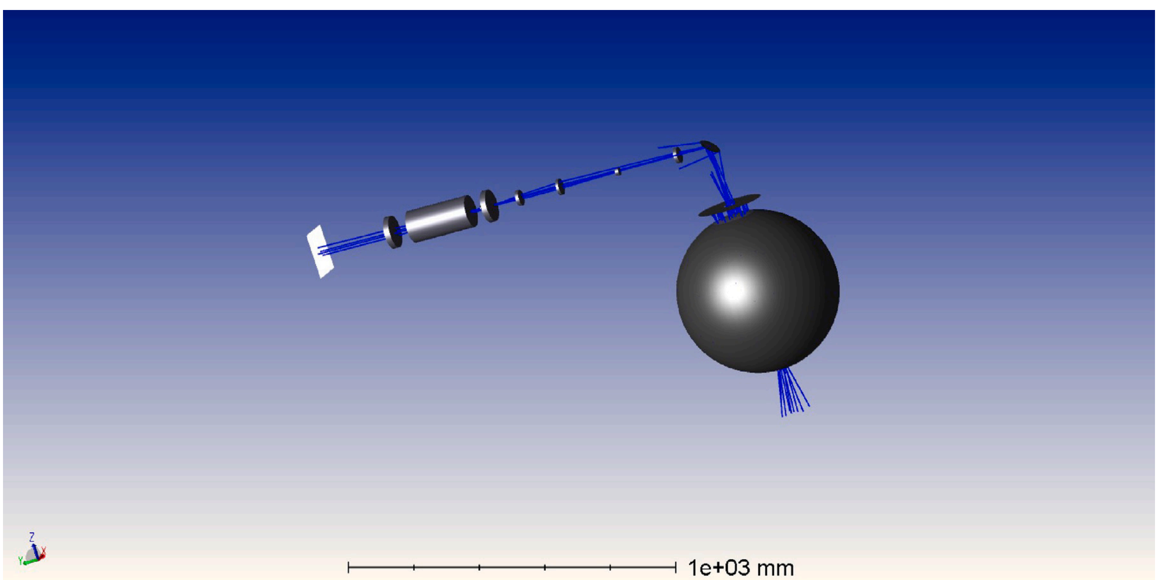

Fig. 13. Shaded model.

where

$$I_{max} = \frac{A^2T^2}{(1-R^2)} \tag{2}$$

is the maximum value of the intensity. And

$$F = \frac{4R}{(1-R)^2} \tag{3}$$

is the reflective finesse.

A, T, and R are the amplitudes of the incident light, the transmittivity of the Fabry–Perot etalon and the reflectivity of the etalon surface, respectively. δ is the phase difference between the transmitted rays and is given by

$$\delta = \frac{(2\mu d cos\theta)2\pi}{\lambda} \tag{4}$$

where μ is the refractive index of the media between the plates and λ is wavelength of the incident ray, d is the distance between the plates, and θ is the angle of the incident ray with the normal. So, one can vary the phase between the successive transmitted rays by changing the refractive index of the material between the plates or by changing the inclination of the etalon surface, or the angle of incidence of the rays. In other words, the wavelength scanning of the spectral line profile can be done with one of the above methods. But in practise, it is easy to vary the phase difference by moving one of the plates or by varying the refractive index of the media between the plates. The transmitted beam has a distribution of intensities in periodic fringes with a maximum intensity of I_{max} and the minimum intensity is

$$I_{min} = \frac{A^2T^2}{(1+R^2)} \tag{5}$$

4.1. Theoretical

From Eq. (3),

$$F = \frac{4R}{(1-R)^2} = \frac{4 \cdot 0.85}{(1-0.85)^2} = 151.11 \tag{6}$$

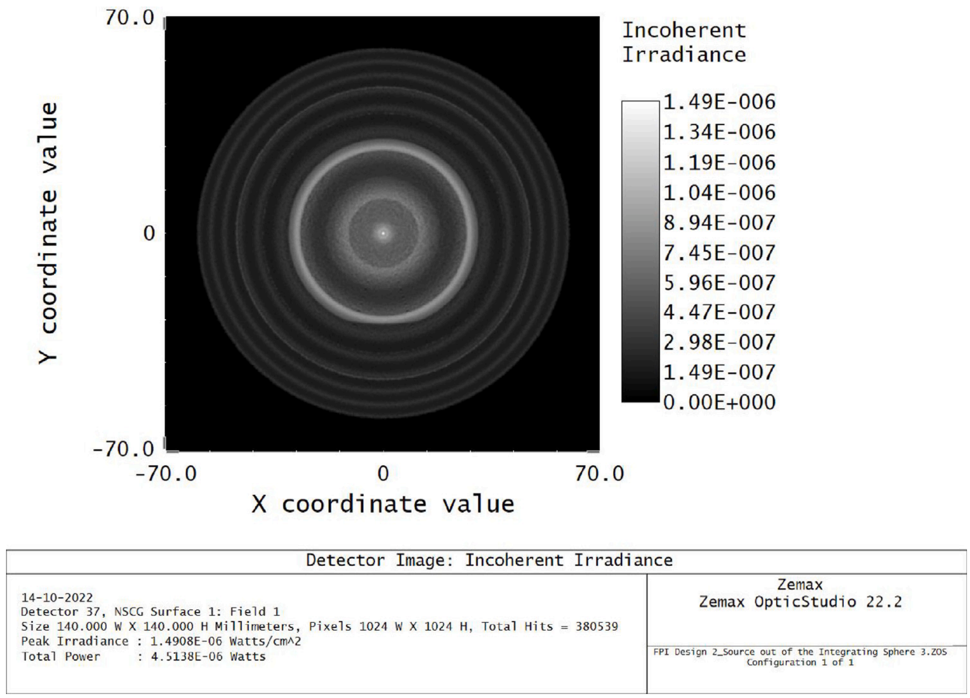

Fig. 14. Detector view.

is the coefficient of finesse, R is the reflectivity of the plates = 85%. High reflectivity results in a high quality factor Q_R (Betzler). Thus a Fabry–Perot interferometer with high Q_R is said to have a high finesse. Accurately knowing this value is useful for approximation.

$$Q_R = \frac{4R}{(1-R)^2} \tag{7}$$

The full width of half maximum (FWHM) is given by

$$FWHM = \gamma = \frac{4}{\sqrt{F}} = \frac{4}{\sqrt{151.11}} = 0.32 \tag{8}$$

Using Eq. (8), the finesse is defined as

$$\mathcal{F} = \frac{2\pi}{\gamma} = \frac{2\pi}{0.32} = 19.6 \tag{9}$$

4.2. Experimental

The value of finesse is calculated by Eq. (10). From Fig. 10, the measurements like the FSR and $\delta\lambda$ are shown in the figure. For the best chosen peaks, the average value of the finesse is found to be 16. Thus, a comparison of the theoretical and experimental finesse shows that the designed optical system delivered the finesse with an accuracy of 80%.

$$\mathcal{F} = \frac{FSR}{\delta\lambda} = 16 \tag{10}$$

5. Optical simulation with Zemax

Simulations have been performed with ZEMAX (OpticStudio) optical design software. Such an exercise allows one to characterize the complex transmission of the Fabry–Perot cavity, requiring minimal effort to analyse its response. Fig. 12 shows the 3D layout, Fig. 13 the shaded model and Fig. 14 shows the detector view. The non-sequential mode was utilized for this purpose. For the etalon, the resonant cavity was the first to be modelled with the coatings capability. The only limitation to the etalon modelling is that the thickness of the layers does not draw on the layout plots. That is in common with the whole coating capability. Other than that, it will react to wavelength and angle changes just fine: as long as 'Use Polarization' is turned on so that coating effects are considered (https://community.zemax.com/got-a-question-7/fabry-perot-cavity-1242).

6. Conclusion

The design that was simulated in ZEMAX (OpticStudio) was further verified experimentally on an optical table. Although the large-sized integrating sphere delivers a good quality of image, the contrast can be further improved at the stage when all the components are assembled into a black anodized metal enclosure housing that is to be deployed in the field for observations. The improvement in image quality can also be achieved by giving a small tilt to the etalon that is mounted on a locally fabricated custom mount. The flipping of the optical filter face did not play a significant role in improving the image quality. However, it is critical to mount the filter exactly perpendicular to the optical axis so as to ensure that the beam is completely transmitted to reach the next component and further on to the etalon.

Declaration of competing interest

The authors declare that they have no known competing financial interests or personal relationships that could have appeared to influence the work reported in this paper.

Data availability

No data was used for the research described in the article

Acknowledgements

The authors would like to thank the engineers and the supporting technical staff of the Indian Institute of Astrophysics, Bengaluru for extending all the necessary support at the stage of fabrication and testing. This development activity was funded by the institute with funds from Dept. of Science and Technology, Govt. of India.

References

Anderson, C., Conde, M., Dyson, P., Davies, T., Kosch, M.J., Thermospheric winds and temperatures above Mawson, Antarctica, observed with an all-sky imaging, Fabry–Perot spectrometer, Ann. Geophys., Copernicus Publications.

Betzler, Klaus., Fabry–Perot Interferometer, FABRYPEROT.TEX KB 20020122, Klaus Betzler.

Gelderman, Richard, Woodgate, Bruce E., Brown, Larry W., 1995. The Goddard Fabry–Perot imager. In: 3D Optical Spectroscopic Methods in Astronomy. In: ASP Conference Series, vol. 71, ISBN: 0-937707-90-2, pp. 89–92.

Hanssen, Leonard M., Snail, Keith A., 2002. Integrating spheres for mid- and near-infrared reflection spectroscopy. In: Chalmers, John M., Griffiths, Peter R. (Eds.), Handbook of Vibrational Spectroscopy. John Wiley & Sons Ltd, Chichester.

Hodgkinson, Jane, Masiyano, Dackson, Tatam, Ralph P., 2009. Using integrating spheres as absorption cells: path-length distribution and application of beer's law. Appl. Opt. 48 (30), 5748–5758. http://dx.doi.org/10.1364/AO.48.005748.

Laufer, Gabriel, 1996. University of Virginia Introduction To Optics and Lasers in Engineering. Cambridge University Press, http://dx.doi.org/10.1017/CBO9781139174190.

Lindseth, I., Bardal, A., Spooren, R., 1999. Spooren reflectance measurements of aluminium surfaces using integrating spheres. Opt. Lasers Eng. 32 (05), 419–435. http://dx.doi.org/10.1016/S0143-8166(00)00010-5.

Pickering, John W., Prahl, Scott A., van Wieringen, Niek, Beek, Johan F., Sterenborg, Henricus J.C.M., van Gemert, Martin J.C., 1993. Double-integrating-sphere system for measuring the optical propermichigan aerospace corporationties of tissue. Appl. Opt. 32 (04), 399–410. http://dx.doi.org/10.1364/AO.32.000399.

Shiokawa, K., Otsuka, Y., Oyama, S., Nozawa, S., Satoh, M., Katoh, Y., Hamaguchi, Y., Yamamoto, Y., Meriwether, J., 2012. Development of low-cost sky-scanning Fabry–Perot interferometers for airglow and auroral studies. Earth Planets Space 64, 1033–1046. http://dx.doi.org/10.5047/eps.2012.05.004.

Wang, Houmao, Yan, Huanhuan, Fu, Liping, Zhang, Xiaoxin, Zong, Weiguo, 2020. Wind retrieval of Fabry–Perot interferometer in the middle and upper atmosphere using wavelength depth method based on satellite-based simulation and ground-based measurement. Eur. J. Remote Sens. 53 (01), 145–155. http://dx.doi.org/10.1080/22797254.2020.1752810.

yuki Yamamoto, Masa, Kubota, Minoru, Takeshita, Shu, Ishii, Mamoru, Murayama, Yasuhiro, Ejiri, Masaki, 2002. Calibration of CRL all-sky imagers using an integrating sphere. Adv. Polar Upper Atmos. Res. 16, 173–180.